



Serial optical coherence scanning reveals an association between cardiac function and the heart architecture in the aging rodent heart

ALEXANDRE CASTONGUAY,^{1,*} JOËL LEFEBVRE,¹ PHILIPPE POULIOT,^{1,2}
PRAMOD AVTI,³ MOHAMMAD MOEINI,^{1,2} AND FRÉDÉRIC LESAGE^{1,2}

¹École Polytechnique de Montréal, C.P. 6079, Succ. Centre-ville, Montréal QC, H3C3A7, Canada

²Institut de Cardiologie de Montréal, 5000 rue Bélanger Est, Montréal, QC, H1T1C8, Canada

³Department of Biophysics, Postgraduate Institute of Medical Education and Research, Chandigarh, 160012, India

*alexandreacastonguay87@gmail.com

Abstract: Normal aging is accompanied by structural changes in the heart architecture. To explore this remodeling, we used a serial optical coherence tomography scanner to image entire mouse hearts at micron scale resolution. *Ex vivo* hearts of 7 young (4 months) and 5 old (24 months) C57BL/6 mice were acquired with the imaging platform. OCT of the myocardium revealed myofiber orientation changing linearly from the endocardium to the epicardium. In old mice, this rate of change was lower when compared to young mice while the average volume of old mice hearts was significantly larger ($p < 0.05$). Myocardial wall thickening was also accompanied by extracellular spacing in the endocardium, resulting in a lower OCT attenuation coefficient in old mice endocardium ($p < 0.05$). Prior to serial sectioning, cardiac function of the same hearts was imaged *in vivo* using MRI and revealed a reduced ejection fraction with aging. The use of a serial optical coherence tomography scanner allows new insight into fine age-related changes of the heart associated with changes in heart function.

© 2017 Optical Society of America

OCIS codes: (170.4500) Optical coherence tomography; (170.6935) Tissue characterization; (170.6900) Three-dimensional microscopy; (170.2655) Functional monitoring and imaging.

References and links

1. E. G. Lakatta and D. Levy, "Arterial and Cardiac Aging: Major Shareholders in Cardiovascular Disease Enterprises: Part I: Aging Arteries: A "Set Up" for Vascular Disease," *Circulation* **107**(1), 139–146 (2003).
2. E. G. Lakatta and D. Levy, "Arterial and Cardiac Aging: Major Shareholders in Cardiovascular Disease Enterprises: Part II: The Aging Heart in Health: Links to Heart Disease," *Circulation* **107**(2), 346–354 (2003).
3. D. Levy, R. J. Garrison, D. D. Savage, W. B. Kannel, and W. P. Castelli, "Prognostic Implications of Echocardiographically Determined Left Ventricular Mass in the Framingham Heart Study," *N. Engl. J. Med.* **322**(22), 1561–1566 (1990).
4. A. W. Haider, M. G. Larson, E. J. Benjamin, and D. Levy, "Increased left ventricular mass and hypertrophy are associated with increased risk for sudden death," *J. Am. Coll. Cardiol.* **32**(5), 1454–1459 (1998).
5. S. P. Schulman, E. G. Lakatta, J. L. Fleg, L. Lakatta, L. C. Becker, and G. Gerstenblith, "Age-related decline in left ventricular filling at rest and exercise," *Am. J. Physiol.* **263**(6 Pt 2), H1932–H1938 (1992).
6. C. J. Swinne, E. P. Shapiro, S. D. Lima, and J. L. Fleg, "Age-associated changes in left ventricular diastolic performance during isometric exercise in normal subjects," *Am. J. Cardiol.* **69**(8), 823–826 (1992).
7. D. D. Streeter, Jr., H. M. Spotnitz, D. P. Patel, J. Ross, Jr., and E. H. Sonnenblick, "Fiber Orientation in the Canine Left Ventricle during Diastole and Systole," *Circ. Res.* **24**(3), 339–347 (1969).
8. B. Taccardi, E. Macchi, R. L. Lux, P. R. Ershler, S. Spaggiari, S. Baruffi, and Y. Vyhmeister, "Effect of myocardial fiber direction on epicardial potentials," *Circulation* **90**(6), 3076–3090 (1994).
9. D. D. Streeter, Jr. and W. T. Hanna, "Engineering mechanics for successive states in canine left ventricular myocardium. II. Fiber angle and sarcomere length," *Circ. Res.* **33**(6), 656–664 (1973).
10. G. J. Strijkers, A. Bouts, W. M. Blankesteyn, T. H. J. M. Peeters, A. Vilanova, M. C. van Prooijen, H. M. H. F. Sanders, E. Heijman, and K. Nicolay, "Diffusion tensor imaging of left ventricular remodeling in response to myocardial infarction in the mouse," *NMR Biomed.* **22**(2), 182–190 (2009).
11. A. Brooks, V. Schinde, A. C. Bateman, and P. J. Gallagher, "Interstitial fibrosis in the dilated non-ischaemic myocardium," *Heart* **89**(10), 1255–1256 (2003).

12. I. J. LeGrice, B. H. Smaill, L. Z. Chai, S. G. Edgar, J. B. Gavin, and P. J. Hunter, "Laminar structure of the heart: ventricular myocyte arrangement and connective tissue architecture in the dog," *Am. J. Physiol.* **269**(2 Pt 2), H571–H582 (1995).
13. D. D. Streeter and D. L. Bassett, "An engineering analysis of myocardial fiber orientation in pig's left ventricle in systole," *Anat. Rec.* **155**, 503–511 (1966).
14. D. F. Scollan, A. Holmes, R. Winslow, and J. Forder, "Histological validation of myocardial microstructure obtained from diffusion tensor magnetic resonance imaging," *Am. J. Physiol.* **275**(6 Pt 2), H2308–H2318 (1998).
15. T. G. Reese, R. M. Weisskoff, R. N. Smith, B. R. Rosen, R. E. Dinsmore, and V. J. Wedeen, "Imaging myocardial fiber architecture in vivo with magnetic resonance," *Magn. Reson. Med.* **34**(6), 786–791 (1995).
16. D. E. Sosnovik, R. Wang, G. Dai, T. G. Reese, and V. J. Wedeen, "Diffusion MR tractography of the heart," *J. Cardiovasc. Magn. Reson.* **11**, 47 (2009).
17. D. E. Sosnovik, C. Mekkaoui, S. Huang, H. H. Chen, G. Dai, C. T. Stoeck, S. Ngoy, J. Guan, R. Wang, W. J. Kostis, M. P. Jackowski, V. J. Wedeen, S. Kozerke, and R. Liao, "Microstructural impact of ischemia and bone marrow-derived cell therapy revealed with diffusion tensor magnetic resonance imaging tractography of the heart in vivo," *Circulation* **129**(17), 1731–1741 (2014).
18. W. Li, M. Lu, S. Banerjee, J. Zhong, A. Ye, J. Molter, and X. Yu, "Ex vivo diffusion tensor MRI reflects microscopic structural remodeling associated with aging and disease progression in normal and cardiomyopathic Syrian hamsters," *NMR Biomed.* **22**(8), 819–825 (2009).
19. C. J. Goergen, H. Radhakrishnan, S. Sakadžić, E. T. Mandeville, E. H. Lo, D. E. Sosnovik, and V. J. Srinivasan, "Optical coherence tractography using intrinsic contrast," *Opt. Lett.* **37**(18), 3882–3884 (2012).
20. C. P. Fleming, C. M. Ripplinger, B. Webb, I. R. Efimov, and A. M. Rollins, "Quantification of cardiac fiber orientation using optical coherence tomography," *J. Biomed. Opt.* **13**(3), 030505 (2008).
21. C. J. Goergen, H. H. Chen, S. Sakadžić, V. J. Srinivasan, and D. E. Sosnovik, "Microstructural characterization of myocardial infarction with optical coherence tractography and two-photon microscopy," *Physiol. Rep.* **4**(18), e12894 (2016).
22. C. M. Ambrosi, V. V. Fedorov, R. B. Schuessler, A. M. Rollins, and I. R. Efimov, "Quantification of fiber orientation in the canine atrial pacemaker complex using optical coherence tomography," *J. Biomed. Opt.* **17**(7), 071309 (2012).
23. C. Fan and G. Yao, "Imaging myocardial fiber orientation using polarization sensitive optical coherence tomography," *Biomed. Opt. Express* **4**(3), 460–465 (2013).
24. Y. Wang and G. Yao, "Optical tractography of the mouse heart using polarization-sensitive optical coherence tomography," *Biomed. Opt. Express* **4**(11), 2540–2545 (2013).
25. Y. Wang, K. Zhang, N. B. Wasala, X. Yao, D. Duan, and G. Yao, "Histology validation of mapping depth-resolved cardiac fiber orientation in fresh mouse heart using optical polarization tractography," *Biomed. Opt. Express* **5**(8), 2843–2855 (2014).
26. J. Lefebvre, A. Castonguay, P. Pouliot, M. Descoteaux, and F. Lesage, "Whole mouse brain imaging using optical coherence tomography: reconstruction, normalization, segmentation, and comparison with diffusion MRI," *Neurophotonics* **4**(4), 041501 (2017).
27. S. P. Amato, F. Pan, J. Schwartz, and T. M. Ragan, "Whole Brain Imaging with Serial Two-Photon Tomography," *Front. Neuroanat.* **10**, 31 (2016).
28. T. Ragan, L. R. Kadir, K. U. Venkataraju, K. Bahlmann, J. Sutin, J. Taranda, I. Arganda-Carreras, Y. Kim, H. S. Seung, and P. Osten, "Serial two-photon tomography for automated ex vivo mouse brain imaging," *Nat. Methods* **9**(3), 255–258 (2012).
29. H. Wang, J. Zhu, and T. Akkin, "Serial optical coherence scanner for large-scale brain imaging at microscopic resolution," *Neuroimage* **84**, 1007–1017 (2014).
30. H. Wang, A. J. Black, J. Zhu, T. W. Stigen, M. K. Al-Qaisi, T. I. Netoff, A. Abosch, and T. Akkin, "Reconstructing micrometer-scale fiber pathways in the brain: Multi-contrast optical coherence tomography based tractography," *Neuroimage* **58**(4), 984–992 (2011).
31. P. J. Cassidy, J. E. Schneider, S. M. Grieve, C. Lygate, S. Neubauer, and K. Clarke, "Assessment of motion gating strategies for mouse magnetic resonance at high magnetic fields," *J. Magn. Reson. Imaging* **19**(2), 229–237 (2004).
32. J. E. Schneider, P. J. Cassidy, C. Lygate, D. J. Tyler, F. Wiesmann, S. M. Grieve, K. Hulbert, K. Clarke, and S. Neubauer, "Fast, high-resolution in vivo cine magnetic resonance imaging in normal and failing mouse hearts on a vertical 11.7 T system," *J. Magn. Reson. Imaging* **18**(6), 691–701 (2003).
33. A. Castonguay, P. K. Avti, M. Moieni, P. Pouliot, M. S. Tabatabaei, S. Bélanger, and F. Lesage, "Investigating the correlation between white matter and microvasculature changes in aging using large scale optical coherence tomography and confocal fluorescence imaging combined with tissue sectioning," in D. L. Farkas, D. V. Nicolau, and R. C. Leif, eds. (2015), p. 93281M.
34. F. Lesage, A. Castonguay, P. L. Tardif, J. Lefebvre, and B. Li, "Investigating the impact of blood pressure increase to the brain using high resolution serial histology and image processing," in M. Papadakis, V. K. Goyal, and D. Van De Ville, eds. (2015), p. 95970M.
35. P.-L. Tardif, M.-J. Bertrand, M. Abran, A. Castonguay, J. Lefebvre, B. E. Stähli, N. Merlet, T. Mihalache-Avram, P. Geoffroy, M. Mecteau, D. Busseuil, F. Ni, A. Abulrob, É. Rhéaume, P. L'Allier, J.-C. Tardif, and F. Lesage, "Validating Intravascular Imaging with Serial Optical Coherence Tomography and Confocal Fluorescence Microscopy," *Int. J. Mol. Sci.* **17**(12), 2110 (2016).

36. K. A. Vermeer, J. Mo, J. J. A. Weda, H. G. Lemij, and J. F. de Boer, "Depth-resolved model-based reconstruction of attenuation coefficients in optical coherence tomography," *Biomed. Opt. Express* **5**(1), 322–337 (2013).
37. M. Hohmann, B. Lengenfelder, R. Kanawade, F. Klämpfl, and M. Schmidt, "Extension of depth-resolved reconstruction of attenuation coefficients in optical coherence tomography for slim samples," in T. Omatsu, Y. Hayasaki, Y. Ogura, Y. Ozeki, and S. Ohno, eds. (2015), p. 97920P.
38. E. Heiberg, J. Sjögren, M. Ugander, M. Carlsson, H. Engblom, and H. Arheden, "Design and validation of Segment—freely available software for cardiovascular image analysis," *BMC Med. Imaging* **10**, 1 (2010).
39. N. Otsu, "A Threshold Selection Method from Gray-Level Histograms," *IEEE Trans. Syst. Man Cybern.* **9**, 62–66 (1979).
40. G. Gerstenblith, J. Frederiksen, F. C. Yin, N. J. Fortuin, E. G. Lakatta, and M. L. Weisfeldt, "Echocardiographic assessment of a normal adult aging population," *Circulation* **56**(2), 273–278 (1977).
41. A. Mosterd, A. W. Hoes, M. C. de Bruyne, J. W. Deckers, D. T. Linker, A. Hofman, and D. E. Grobbee, "Prevalence of heart failure and left ventricular dysfunction in the general population; The Rotterdam Study," *Eur. Heart J.* **20**(6), 447–455 (1999).

1. Introduction

The incidence and prevalence of cardiovascular diseases increase with aging [1]. Normal aging of the heart is associated with changes in its architectural morphology [2]. Furthermore, left ventricular (LV) hypertrophy is associated with increasing age, which is known to increase the risk of stroke and cardiovascular disease in [3,4]. During aging, the mechanical function of the heart is also affected [5,6]. Among potential transducers of these changes, the organization of myocardial fibers plays a key role in mechanical and electrical function [7,8]. Histology has revealed a cross-helical structure in the heart muscle, whereas myofibers in the epicardium form a left-handed helix and myofibers in the endocardium form a right-handed helix [9]. Myofiber disorganization jeopardizes normal heart function and is known to result in cardiovascular disorders such as myocardial infarction [10].

Histology has widely been used to investigate the heart morphology at the cellular level [7,9,11–13]. However, histological studies only provide a small representation of the entire heart and do not access microstructural organization in the intact organ. Magnetic resonance imaging (MRI) has emerged as a tool to image the intact heart both *ex vivo* [14] and *in vivo* [15]. Diffusion tensor MRI (DTI) allows for 3D characterization of the myocardium structure [16–18]. However, DTI imaging has a limited spatial resolution (typically not better than 50µm), which is not sufficient to reveal the heart microstructure in details, especially when studying mouse models which are widely used in cardiovascular research.

High resolution optical coherence tomography (OCT) has emerged as a proficient tool to image cardiac tissue [19,20]. OCT imaging is based on backscattered signal from tissue to obtain depth-resolved information and does not rely on exogenous contrast agents. The high spatial resolution of OCT, typically of the order of a few micrometers, allows visualization of microstructural details of heart muscle fibers. Native OCT contrast has been used to characterize myocardial fiber orientation using *en face* 2D planes in the mouse heart [21,22]. Others have used polarization-sensitive OCT systems to measure local retardance and thus obtain fiber orientation along the optical axis [23–25]. However, limited light penetration in biological tissue and the small imaging field of view allowed by microscopic imaging limits our ability to image the entire heart. Thus, obtaining a highly-resolved OCT data set of the entire mouse heart remains challenging.

To overcome this challenge, we recently developed a motorized serial OCT scanner to sequentially slice through agarose embedded tissue [26]. Serial histology imaging scanners have been demonstrated in recent years [27,28] as a technique able to image entire small organs at microscopic resolution and have been combined to many imaging modalities including OCT [29,30]. This system allows block-face imaging of large sections of exposed intact tissue, before removing a thin slice with a vibratome, exposing new tissue to image. Each slice is serially scanned to image every sub-region of a large surface. Post-processing algorithms are then used to reconstruct a 3D data set of the entire small animal organ.

With this system, we can image entire mouse hearts with little human intervention and in a time-lapse of only a few hours, thus allowing group-wise studies. The aim of this study was to use the developed OCT serial scanner to investigate morphological changes in the heart architecture that occur with normal aging. We show that the heart volume increases with age due to the thickening of the left ventricle wall. 2D orientation distribution function (ODF) estimation was also performed in the entire mouse heart, providing estimates of the myofiber transverse angle. Results show that the slope of fiber orientation versus wall depth changes with age. In the same animals, and prior to serial sectioning, *in vivo* MRI imaging of the heart revealed a reduced ejection fraction with aging, suggesting that changes in heart architecture are linked to heart efficiency.

2. Methods

The Animal Research Ethics Committee of the Montreal Heart Institute approved all procedures, in accordance with the Canadian Council on Animal Care recommendations. A total of 12 mice (C57B16) were used in this study categorized into 2 groups: young mice (4 months old, $n = 7$) and aged mice (24 months old, $n = 5$).

2.1 MRI cardiac imaging

Cardiac CINE MRI was performed on a 30 cm 7T horizontal MR scanner (Agilent, Palo Alto, CA) with mice in prone position, with a 12 cm inner diameter gradient coil insert (gradient strength 600 mT/m, rise-time 130 μ s). A 4-channel receive only surface coil positioned under the mouse was used in combination with a quadrature transmit/receive birdcage coil with an internal diameter of 69 mm (RAPID Biomedical, Germany). Anesthesia was maintained with 2.0-2.5% isoflurane in pure oxygen and body temperature was maintained at 37.0°C using a warm air fan (SA Instruments, Stony Brook, NY). ECG was recorded via two metallic needles placed subcutaneously near the heart under the armpits. A pressure transducer for respiratory gating was placed under the abdomen near the sternum. The animal was then positioned into the MRI and a combination of manual and automatic shimming was used to shim over the heart region. Scout images were obtained for choosing heart short axis slices. A CINE sequence was run with simultaneous ECG triggering and respiration gating (double gating), while maintaining the steady-state [31,32], with effective TR equal to the RR-interval, TE = 1.4 ms, 16 cardiac time frames, FOV 30x30 mm, matrix size 192x192, slice thickness 0.8 mm, no gap, flip angle 20 degrees, 8 averages, 147 kHz acquisition bandwidth, 10 short axis slices covering the whole left ventricle, for an acquisition time of 33 minutes.

2.2 Ex vivo tissue preparation

Animals were anesthetized under 2% isoflurane and transcardially perfused through the apex of the heart with 20 mL of saline, followed by 20 mL of 4% paraformaldehyde (PFA) in phosphate buffer saline (PBS) at a rate of 2 mL/min. The heart was carefully extracted and submerged in 4% PFA. Each mouse heart was suspended upside down, with the apex facing up, in a 4% oxidized agarose block [28] using a custom holder before serial imaging.

2.3 Serial OCT imaging

A custom build automated serial histology scanner combined with swept-source optical coherence tomography (SS-OCT) microscope was used to image the agarose embedded mouse hearts. The developed SS-OCT setup was reported in previous work [26,33–35]. Briefly, a vibratome is used to sequentially slice through the agarose embedded samples to expose new tissue to image (Fig. 1(a)). Linear stage motors are used to move the sample relative to the objective to image every sub-region of the exposed tissue plane. After imaging each section, a vertical stage raises the sample to remove a 200 μ m thick slice of already imaged tissue. The vertical position is adjusted to have the focus of the objective at 100 μ m under the tissue surface, thus imaging intact tissue.

The OCT microscope uses a fibered swept-source laser ($\lambda = 1310 \pm 100$ nm) with a 50kHz sweep rate (Axsun, 1310 Swept Source Engine) to capture OCT volumetric data sets of 512 B-scans with 512 A-lines each in around 5 seconds. The beam exiting the fiber is enlarged with a telescope ($f_1 = 35$ mm, $f_2 = 100$ mm) to fill the pupil of a 3x telecentric objective (Thorlabs, LSM04), which is used to scan the surface of the tissue using a pair of galvanometric mirrors. This low magnification objective allowed to image large field of views (2.5×2.5) mm with a measured lateral resolution of $8\mu\text{m}$ in water. A custom-made coverslip was used to transition from air surrounding the microscope objective to water surrounding the submerged sample, to preserve the same water thickness in each image and to avoid water ripples. Refractive index matched glass was used in the reference arm to compensate dispersion in optical components and allowed to have an axial resolution of $10\mu\text{m}$ in water. To save hard drive space, highly attenuated and out of focus volumetric data at a depth over $780\mu\text{m}$ was discarded.

Post-processing algorithms were developed to reconstruct 3D OCT volumetric data sets. Briefly, the computation of the phase-correlation of all neighboring tiles within a mosaic plane allowed to estimate the position of every imaged sub-region. Next, linear blending of overlapping tiles was used to stitch together all volumes for each slice. Finally, slices were stitched together along the axial direction by computing the shift between adjacent slices using the cross-correlation of the 2D image gradient and were fused using linear blending. The reconstruction gave rise to a 3D data set of optical reflectivity in heart tissue. The axial PSF was extracted from the data and used to compensate for the objective's signal variation along the depth axis. To compensate attenuation in biological tissue, the depth dependent signal intensity attenuation due to light scattering and absorption was also corrected using a single scattering photon model to estimate local attenuation coefficient [36,37]. Details regarding the OCT data reconstruction and attenuation compensation can be found in [26].

2.4 MRI data analysis

Ejection fraction (EF) and left ventricle mass were estimated by manually segmenting the left ventricle in MRI images using the software Segment (Medviso, Lund University [38]). Papillary muscles and the apex slice were excluded from the segmentations. The average heart rate (HR) during the cardiac CINE scan was calculated retrospectively from the physiological data, allowing an estimate of the cardiac output (CO).

2.5 OCT data analysis

OCT data sets were collected from 12 mice and fiber orientation within the entire left ventricle was of interest. For 2D orientation estimations, we took an average intensity projection (AIP) over $200\mu\text{m}$ around the focus for each tissue slice to enhance the myofiber structure. As described in [19], a 2D discrete Fourier transform (DFT) over areas of $(200 \times 200)\mu\text{m}$ was calculated after multiplication by a symmetric Hanning window. The local orientation distribution function (ODF) was obtained by summing the high-pass filtered 2D DFT slice magnitude squared at each angle:

$$ODF(\theta) = \int_{-\infty}^{\infty} \left| F_w(f_x, f_y) \right|^2 H(f_x, f_y) df \quad (1)$$

where f_x is $-f \sin \theta$, f_y is $f \cos \theta$, F_w is the windowed Fourier transform and H is a high-pass filter. The maximum of the ODF indicates the dominant fiber orientation, which was, by definition, between -90° and 90° . ODFs were measured over entire slices by steps of $25\mu\text{m}$ to obtained large scale 2D orientation maps. To express fiber orientation in polar coordinates, we defined the origin relative to the epicardial surface of the heart. Fiber orientation values are thus expressed in terms of the radial position relative to the center of the slice.

To measure the heart volume, previously constructed AIPs over $200\ \mu\text{m}$ for each slice were masked. First, the 2D AIPs edges were enhanced by subtracting a morphological dilation of the original image to its morphological erosion. Dilation and erosion were generated using a disk of radius $25\ \mu\text{m}$. The resulting edge enhanced image was segmented in two classes using the watershed algorithm such as: pixels with value lower than 5% of the maximum were marked as (1) and pixels with value above the threshold value based on Otsu's method [39] were marked as (2). The resulting heart muscle mask excludes the lumen of the ventricles. Considering a resolution of $(4.88 \times 4.88 \times 200)\ \mu\text{m}$ for AIPs, we can measure the slice volume by counting pixels within the heart mask.

3. Results

3.1 Serial OCT images

Following embedding, hearts could be automatically imaged consistently on the serial OCT scanner and reconstructed with high quality (Fig. 1). 3D volumes were then used to yield either short or long axis views with no noticeable artefacts. The imaging platform could image the entire ventricles of the heart, revealing a higher contrast in the midwall of the left ventricle.

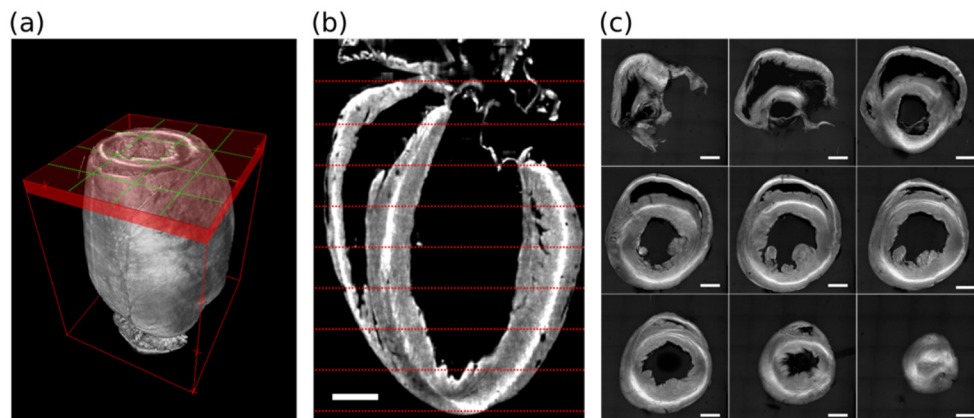


Fig. 1. Heart reconstruction from serial OCT imaging. (a) Schematic of the heart positioning for serial sectioning. Red borders delimit the volume acquired by the system. Red area shows volumetric data imaged by one serially scanned section with green lines delimiting adjacent tiles imaged by the microscope. (b) Long axis view of the heart showing left and right ventricles. Red lines show position of short axis views in (c). (c) short axis views spaced by one millimeter. Scale bar: 1mm.

When focusing on average intensity projections over short axis slices (Fig. 2(b)), the structure of myocardial fibers was clearly identified and enabled ODF estimation on a pixel by pixel basis. Focusing on small regions, one can identify the orientation of myocardial fibers (Fig. 2(c)i-iii)). Estimations based on the ODFs were used to generate maps of transverse orientation across the whole slice. ODFs over entire short axis views revealed the particular organization in myocardial fibers, whereas fibers in the epicardium show a left-handed organization and fibers in the endocardium a right-handed orientation. Note that Fig. 2 shows short axis slices as viewed from the apex, inverting the left/right handed organization of endo/epicardium. Color coding the fiber orientation gave rise to swirl-like images of the short axis views over the whole heart (Fig. 2(d-e)). Converting fiber orientation to polar coordinates relative to the center of the short axis slices shows a varying fiber orientation with wall depth (Fig. 2(f)). Polar angle was inverted to respect fiber orientation convention where short axis are viewed from the base. The polar coordinate system allowed measurement of relative fiber orientation with wall depth (Fig. 2(g)) and wall thickness relative to angular

position (Fig. 2(h)). The center of each short axis slices was determined from the tissue mask by consecutive morphological erosions until a single pixel remained.

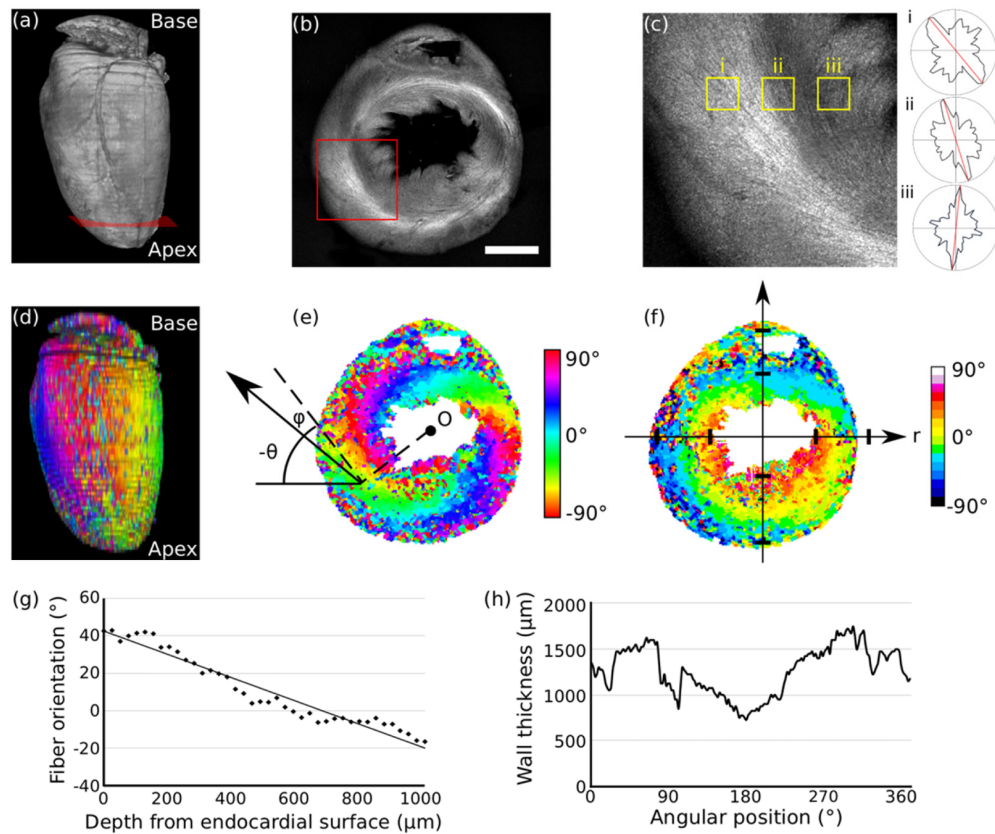


Fig. 2. Myofiber architecture. (a) 3D representation of a young mouse heart. (b) short axis AIP over 200µm around red plane depicted in (a). Scale bar: 1mm. (c) Detailed view of region presented in (b) with ODFs showing preferred orientation in region of interest of (200 x 200) µm. (d) 3D in plane orientation of heart shown in (a). (e). In plane orientation of short axis view in (b). Arrow shows local fiber oriented at an angle described in Cartesian coordinates (θ) and in polar coordinates (φ) relative to the center O of the slice. (f) Fiber orientation converted to polar coordinates, relative to the center of the slice. r : distance to the center. (g) Average fiber orientation along depth from endocardial surface for the slice presented in (f). Fitted line to the measured data shows an orientation change of $0.07^\circ/\mu\text{m}$. (h) Left ventricle wall thickness as a function of the radial position of slice in (f).

3.2 Age dependent changes in myocardial fiber organization

Consolidating data across all hearts, we investigated age-related changes in left ventricle volume and rate of orientation change as a function of radial distance (Fig. 3). Transverse fiber orientation changes were higher near the apex of the heart and decreased at 4mm from the apex. The fiber orientation changes at a given distance from the apex were measured over the entire short axis plane. Left ventricle wall thickness averaged at 1.1mm close to the apex and rose to 1.5 mm at 4mm from the apex for both age groups (Fig. 3(b)). As expected, we measured a significant change ($p < 0.05$) in ventricle volume, increasing with age (Fig. 3(d)). The change in ventricular volume, more specifically a thickening the ventricle wall, was more apparent at 1-2mm from the apex. Expansion of ventricle volume was accompanied by a reorganization of the myocardial fibers along their angular direction with reduced orientation change as a function of distance (Fig. 3(a)). A paired t -test showed that there was a significant

difference in orientation change for matched distances from the apex ($p < 0.01$). Looking at the total change in orientation, we observed that the average angle at the endocardial surface (4 months: $38.4 \pm 0.8^\circ$ / 24 months: $38.2 \pm 0.3^\circ$) and at the epicardial surface (4 months: $-32.3 \pm 0.4^\circ$ / 24 months: $-31.6 \pm 0.3^\circ$) remained similar for both age groups.

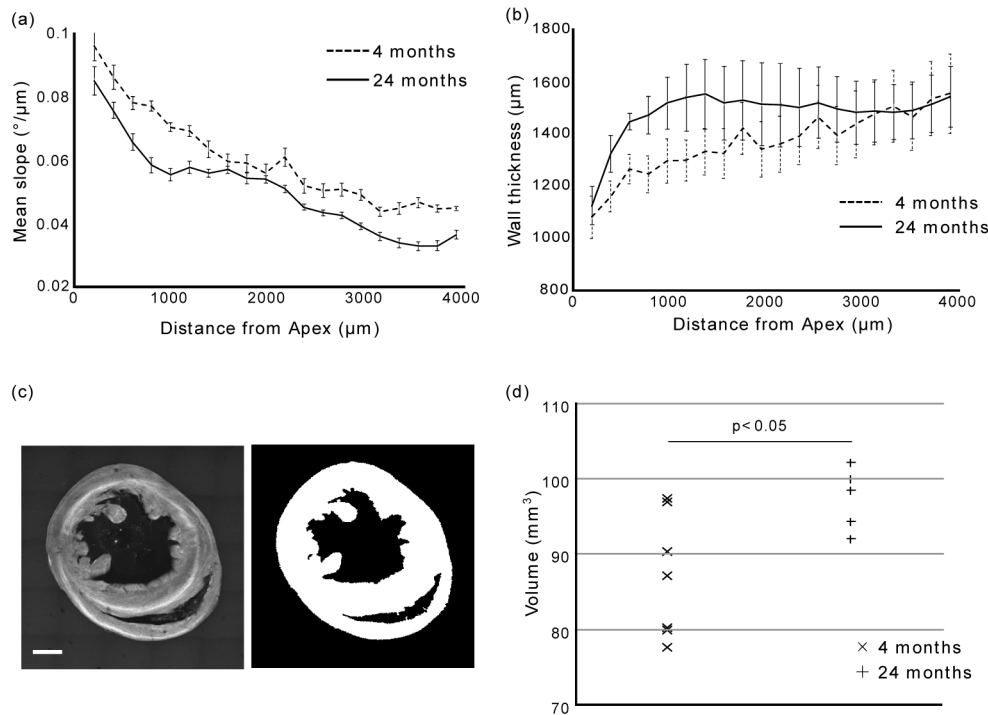


Fig. 3. Age dependent changes in heart architecture. (a) Average myofiber orientation changes as a function of distance from apex for young and aged mice. A paired t-test showed a significant ($p < 0.01$) orientation difference between young and old mice. (b) Average left ventricle wall thickness as a function of distance from the apex for young and old mice. (c) Tissue masking of a short axis view. (d) Heart volume up to 4mm from the apex measured from masked AIPs. A significant heart volume increase was observed in old mice ($p < 0.05$). Error bar in (a) and (b) show standard error.

Visual qualitative inspections of short axis views reveal extracellular space within the endocardium of old mice (Fig. 4(a), green arrows). These extracellular spaces exhibit a low OCT reflectivity contrast, akin to the signal contrast within the ventricle cavity. To further quantify this change, we measured tissue OCT attenuation slopes within specific regions of interest of the endocardium (Fig. 4(b)). For attenuation coefficient measurements, data sets did not undergo the correction for single scattering photon model. When comparing all 12 mice, we observed a significant difference ($p < 0.05$) between young and old hearts (Fig. 4(c)) the latter being less attenuating (4 months: $18.6 \pm 1.3 \text{ cm}^{-1}$ / 24 months: $15.4 \pm 0.9 \text{ cm}^{-1}$).

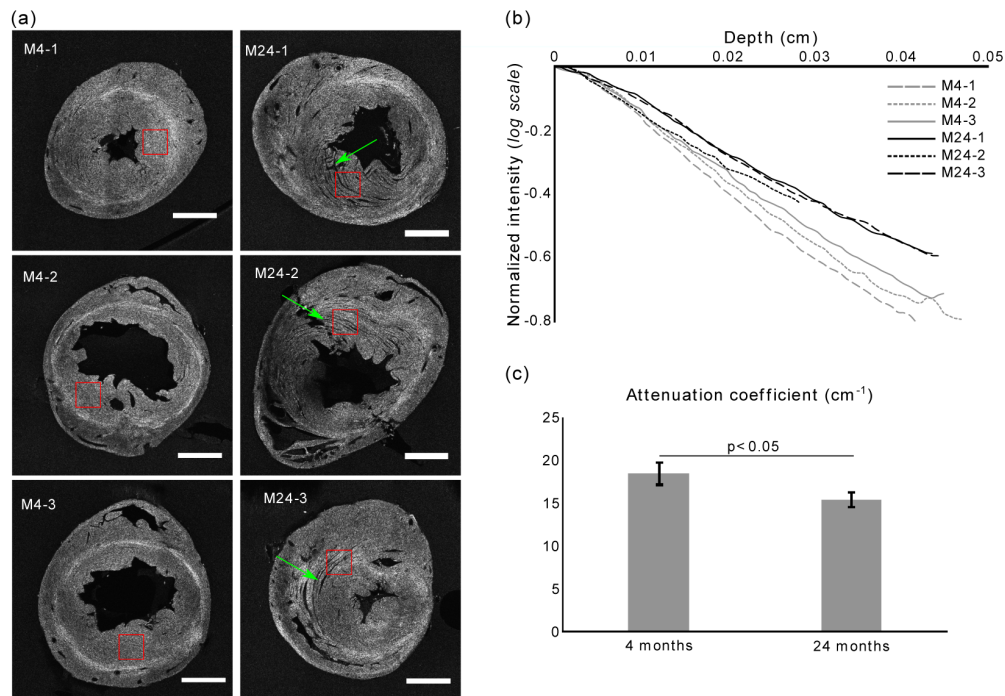


Fig. 4. Light attenuation. (a) Short axis views taken at 1mm from apex from three young mice (left) and three old mice (right). Red boxes of (500x500) μm were used to evaluate tissue attenuation. Scale bar: 1mm. (b) Tissue attenuation from regions of interest in (a). Grey lines: 4 months mice. Black lines: 24 months mice. (c) When looking at all mice, light attenuation in endocardium showed a significant decrease ($p < 0.05$) in old mice.

The next question was whether this change in myocardial fiber structure would lead to changes in heart function or whether it was an adaptation aiming to preserve function in healthy aging mice. CINE MRI data allowed imaging of the heart at different time points to view the whole cycle of the heartbeat. For both mice age groups, the end-systole (ES) and end-diastole (ED) timeframes were identified. Image contrast of heart muscle was sufficient to segment left ventricle cardiac walls for these two timeframes (Fig. 5(a)). Using Segment (Medviso, Lund University), the maximal LV contraction was estimated for every short axis slices. Contraction was defined as the difference in LV area between ES and ED timeframes for matching axial slices divided by the LV-ED area. Left ventricle contraction was maximal near the apex and gradually reduced as moving towards the base of the heart (Fig. 5(b)). Fiber orientation changes depicted in Fig. 3(a) were plotted against LV-slice contraction ratios for matching distances from the apex (Fig. 5(c)). Linear interpolation between *in vivo* LV-slice contraction ratios was used to compensate the sparse sampling. The change in myofiber orientation was linearly correlated to the LV-contraction ratio. Overall, LV contraction was lower for old mice. Using Segment and the average heart rate during acquisition, acquired via ECG recordings, functional parameters were extracted (Table 1). Between age groups, the left ventricle end-systole volume difference was significant ($p < 0.05$), going down to 13 μL for young mice and as much as 19.8 μL for old mice. This resulted in an ejection fraction that was 68.2% for young mice and 58.2% for old mice, reaching a significant difference ($p < 0.05$). Other parameters, showed no significant changes (Table 1).

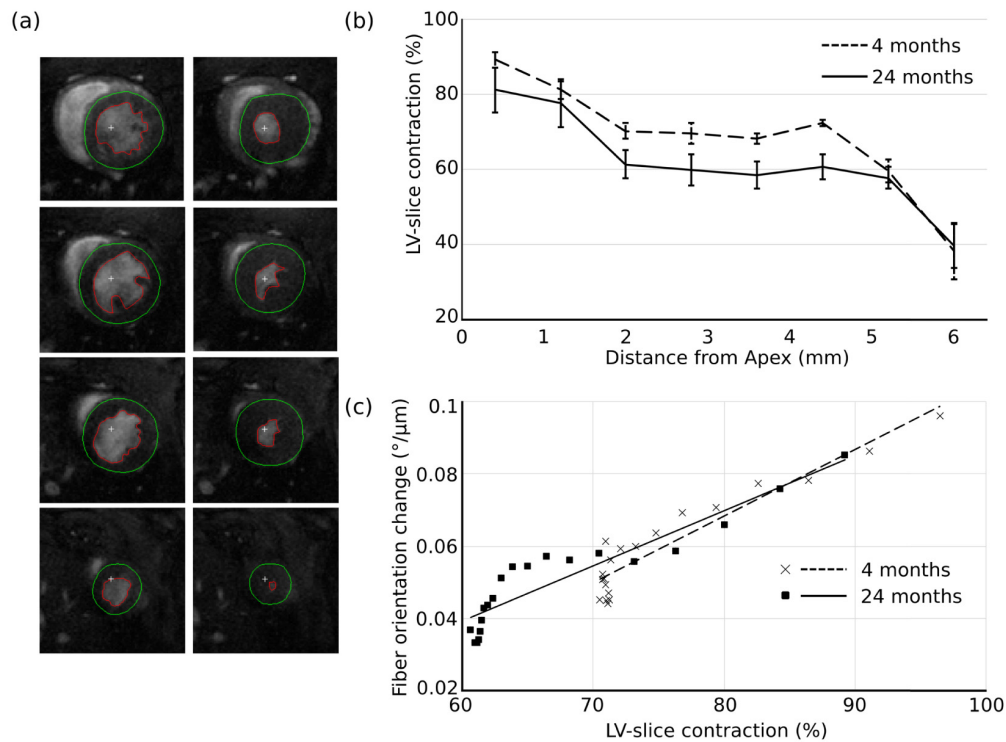


Fig. 5. *In vivo* MRI heart imaging. (a) Example of end-diastole (left) and end-systole (right) timeframes in a young heart. Each image has a field of view of (10x10) mm and 0.8 mm thick. Green lines delimit epicardial surface and red lines show endocardial surface segmented with Segment software. (b) Fraction of left ventricle contraction as a distance from the apex. (c) Fiber orientation change plotted against the LV-slice contraction. Dashed line: linear fit to the 4 months group ($R^2 = 0.885$). Full line: linear fit to the 24 months group ($R^2 = 0.852$)

Table 1. Cardiac functional parameters of two aged groups

Mice ID	LVM (g)	LV-EDV (ul)	LV-ESV (ul)	LV-SV (ul)	LV-EF (%)	HR (bpm)	CO (ml/min)
M4-2	60	43	14	29	67	393	11.4
M4-2	60	46	15	31	67	479	14.8
M4-3	78	43	11	32	74	491	15.7
M4-4	53	42	14	28	67	455	12.7
M4-5	52	36	12	24	67	583	14.0
M4-6	53	36	13	23	64	520	12.0
M4-7	54	41	12	29	71	500	14.5
M4-Average	58.6	41.0	13.0*	28.0	68.2*	488.7	13.6
M24-1	59	40	17	23	58	480	11.0
M24-2	66	47	21	26	55	440	11.4
M24-3	63	50	18	32	64	499	16.0
M24-4	60	59	27	32	54	412	13.2
M24-5	58	39	16	23	59	440	10.1
M24-Average	61.2	47.0	19.8*	27.2	58.0*	454.2	12.4

LVM: Left Ventricle Mass, LV-EDV: Left Ventricle – End Diastole Volume, LV-ESV: Left Ventricle - End Systole Volume, LV-SV: Left Ventricle - Stroke Volume, LV-EF: Left Ventricle - Ejection Fraction. HR: Heart Rate (beats per minute), CO: Cardiac Output. *: $p < 0.05$

4. Discussion

Serial OCT scanning has proven to be an effective method to image the architecture of the mouse heart. Highly resolved optical reflectivity maps combined with wide range scanning enabled imaging the myocardial fibers of the entire heart at the micrometer scale. The effectiveness of this fully automated technique relies strongly on the ability to obtain repetitive smooth and flat cutting surfaces with the vibratome, which was particularly difficult considering the nature of the heart tissue. First, the empty heart ventricles tend to collapse during vibratome sectioning. Filling the heart ventricles with warm agarose before embedding prevented this issue. Second, the elastic nature of unfrozen blood vessels connected to the heart makes it difficult to obtain a smooth imaging surface. Uncut tissue created shadowing in the focal plane and generated errors when locating the tissue interface. To overcome this inconvenience, the hearts were imaged starting with the apex, whereas the problematic blood vessels were located at the base of the heart. Image quality was thus very much reduced at the base of the heart. Nonetheless, the resulting data sets show highly detailed maps of the left ventricle.

From these data sets, a higher OCT reflectivity appeared in the midwall. This higher contrast could be caused by cross helical structure of the heart. In the midwall, myofibers are mostly circumferential. Therefore, the incident light was perpendicular to the myofibers at the midwall leading to a higher backscattered signal. Away from the midwall, light was incident at an angle with the myofibers, resulting in a smaller backscattering. ODFs revealed the spiral organization of the myofibers in the left ventricle. A window size of (200 x 200) μm was empirically chosen for calculations. The trade-off between resolution and sensitivity determined the optimal window size for ODF calculation. Using smaller windows for ODF calculation would have led to less orientation information and resulted in a reduced sensitivity of effective orientation measurement. The use of a higher magnification would have revealed a higher myofiber contrast [21] and would have permitted measuring ODFs at higher resolution with higher sensitivity. However, this is done at the cost of losing some samples due to increased difficulty in acquiring all sub-elements of the image in focus during autonomous slicing.

When comparing young and aged mice, we saw a significant difference in the change of myofiber orientation from the endocardial to the epicardial surface. The average orientation at each cardiac wall remained constant with age, suggesting that the change in orientation was rather caused by the thickening of the LV wall in old mice. This observed thickening resulted in a significant increase of ventricular volume, which is well documented in the aging human heart [3,40]. To determine the nature of the thickening of the LV wall, we measured OCT light attenuation in the endocardium and showed a significant decrease in old mice. Left ventricle thickening could be due to spacing of myofibers, thus explaining the reduction of attenuation. This proposition is supported by our observations of the expansion of interstitial spacing in aged mice and supported by histological analysis of aging hearts by others [18]. However, one must temper *ex vivo* measurements of LV wall thickening and volumes. Indeed, perfusion of the heart could occur during systole or diastole, thus impacting the LV wall thickness and limiting conclusions that can be pulled from these measurements.

In vivo measurements allowed evaluating the impact of these structural changes on the function of the heart. Cardiac CINE MRI revealed that the left ventricle contraction was more important near the apex and gradually reduced moving towards the base. These results showed a linear correlation between fiber orientation change and the ability of the left ventricle to contract itself. Regions showing a higher fiber orientation change had an increase ability to contract. Overall, *in vivo* measurements showed that the end-systole volume was significantly higher for aged mice. This higher ESV led to a significant reduction of the ejection fraction (EF) with aging. In humans, EF decreases significantly with aging only under exhaustive exercise [41]. Anesthesia used during MRI imaging could cause excessive stress to the mice, mimicking the effort of exercise. Our results suggest that the changes in

myofiber architecture are associated with changes in the heart function. One hypothesis, supported by reduced ejection fraction *in vivo*, is that thickening of the LV and the development of fibrotic tissue changes the slope of myofibers which in turn reduces the heart capability to contract along the perpendicular direction for effective blood ejection.

5. Conclusion

In this study, we used serial optical coherence tomography to image changes in the heart architecture with normal aging in mice. Serial sectioning combines the high resolution achieved with histology and the wide field of view allowed by MRI imaging to give a new tool to investigate subtle changes in the whole heart muscle organization. Our results show that changes in the heart morphology are accompanied with changes in its function, as demonstrated by *in vivo* MRI data analysis. Combining large scale histology to *in vivo* imaging and being able to anatomically register comparable information, we hope to refine the potential of MRI as a diagnostic tool to understand underlying microscopic changes of the heart organization.

Funding

Fonds de Recherche du Québec – Nature et Technologies (FRQNT) (501100003151) attributed to Alexandre Castonguay and Joël Lefebvre.

Natural Sciences and Engineering Research Council of Canada (NSERC) (501100000038) attributed to Philippe Pouliot and Frédéric Lesage.

Canadian Institutes of Health Research (CIHR) (501100000024) attributed to Frédéric Lesage.

Disclosures

The authors declare that there are no conflicts of interest related to this article.